ISSN 2007-9737

Laser Beam Spot Detection: A Comparative Analysis of Machine Vision Algorithms in Low Performance Hardware

Gregorio A. Oropeza-Gomez, Francisco G. Peña-Lecona, Jesús Muñoz-Maciel, J. Onofre Orozco-López, Francisco J. Casillas-Rodríguez, Miguel Mora-Gonzalez*

Centro Universitario de los Lagos, Universidad de Guadalajara, Lagos de Moreno, Mexico

gregorio.oropeza@alumnos.udg.mx,
{franciscog.penal, jesus.munozm, juan.onofre, francisco.casillas, miguel.mora}@academicos.udg.mx,
mmoraglez@gmail.com

Abstract. An Optical Spatial filtering is a opto-mechanical system widely used in advanced optics and has broad applicability in diverse fields. This system is used to archive optimal beam quality in applications like high-power laser beams or optical interferometry removing high-frequency noise and improve beam profiles. The efficacy of the system relies on a correct alignment process, which is a human guided or hand made process. In particular, the alignment of the Airy disk and the pinhole. Despite decades of research into alignment process, advancements are focused in the hand made alignment process and the automatization remains as a significant challenge. Since automating the system depends on finding the exact center of the diffraction pattern, this work is dedicated to solving that specific problem. While superpixel segmentation algorithms achieved lower error rates, two of the evaluated algorithms exhibit reduced processing times compared to the latter. The algorithms applicability is aiming the real time execution in controllers running in low resource hardware. A hybrid approach is under discussion.

Keywords. Superpixels, centroid, connected component labeling, optical spatial filtering, airy disk.

1 Introduction

Achieving peak performance in advanced optical systems is fundamentally predicated upon attaining optimal beam quality. Spatial filtering stands as a fundamental technique for this endeavor, acting as a tool to ensure optical beams quality. The optical spatial filtering is critical for noise reduction and solving problems created by scattering and/or diffraction.

It is suitable for applications like high-power laser systems [3], indispensable for mitigating the detrimental effects of back reflections which can destabilize laser operation and even damage sensitive components and for correcting beam distortions that arise from thermal lensing and other optical imperfections. Similarly, in precision metrology, where the accuracy of interference patterns dictates the fidelity of measurements, spatial filters are paramount for ensuring clean and unambiguous signals, enabling advancements in fields like microscopy [16], gravitational wave detection [1], optical coherence tomography (OCT, a biomedical imaging technique relying on interference for subsurface tissue imaging), or surface metrology with interferometry.

Contemporary approaches to spatial filter optimization predominantly rely on manual alignment of pinhole. This procedure is inherently labor-intensive, often requiring even several hours or intervention by an specialists and it is constrained by limitations in both accuracy and reproducibility. The inherently subjective nature of manual adjustment, compounded by mechanical component drift, may result in sub-optimal filtering outcomes, ultimately diminishing system performance and long-term stability.

Moreover, these manual techniques exhibit poor scalability when applied to advanced and sophisticated optical arrangements or high-throughput

settings. The integration of manual spatial filtering within increasingly automated optical workflows exacerbates these challenges.

In response to the limitations associated with manual spatial filtering, this work is exploring algorithms suitable for automated solutions tailored for next-generation optical technologies and the applicability in not high-performance processing equipment. These Airy disk peak point detector algorithms are a requirement in the development of the automated solutions in optical spatial systems.

This study evaluates multiple machine vision algorithms to determine the most effective solution for real-time control systems based on Airy disk diffraction. The comparison prioritizes computational efficiency and centroid accuracy.

In the next section the state of the art related with spatial filter techniques is presented. Then, the basic theory of the Fourier optics, the border following, the connected component labeling, and the superpixels algorithms applied to optical spatial filter is shown. Then, the methodology to compare algorithms to determinate the most suitable to aligned the spatial filter in real time are presented in section 4. In the last two sections the obtained results and the conclusions are presented.

2 Related Work

Early research on spatial filtering systems established the imperative for precise alignment, with Sasaki et al. [12] pioneering an innovative feedback control mechanism using integrated micromachined pinholes and photodiodes to achieve high alignment accuracies. The integration of distinct and novel alignment techniques has refined the spatial filter alignment performance. The application of lateral shearing interferometry by Wang et al. [15] and deformable mirrors by Li et al. [9] has been shown to effectively ensure precise beam collimation and maintain beam quality. Sharma et al. [13] developed a pinhole alignment method using intensity masks, demonstrating high accuracy with readily implementable experimental setups, and Xiao et al. [17] proposed an automatic focusing system capable of performing defocus corrections with sub-micrometric precision.

Recent innovations in spatial filtering processes have increasingly prioritized automation and machine-assisted adjustments. For instance, Zhang et al. [18] developed a parallel auxiliary adjusting machine that enhanced spatial filter lens alignment, incorporating five-dimensional adjustment functions for optimal positioning. Gawali et al. [5] demonstrated the potential of intracavity photonic crystals as spatial filters, achieving improved beam brightness and enabling novel approaches to beam control in edge-emitting lasers.

While these advancements improve the alignment process, remains in physical arrangements with the objective to improve the manual alignment or basic automation like Sasaki et al. [12], so, their implementation in advanced autonomous alignment systems remains out.

To automate this process, the authors have previously developed methods that employ PID controllers, machine learning, and deep learning [6], [10].

3 Basic Concepts

3.1 Optical Spatial Filter in Fourier Optics

While laser beams are widely used in different applications, some of which require uniform intensity, are susceptible to variations caused by scattering and diffraction arising by the optical medium and introducing noise. To address this problem the optical spatial filter is implemented in the application. The optical spatial filter is an opto-mechanical system composed by a laser beam, a microscope lens and a pinhole.

The pinhole acts as a spatial low-pass filter, effectively stripping away high-spatial-frequency noise by blocking light rays that diverge from the optical axis. Conversely, the fundamental low-frequency components that define the beam's shape are transmitted. When the pinhole is precisely aligned at the focal point on the X-Y plane, this filtering significantly reduces noise, resulting in a more uniform wavefront and improved interferometric precision.

The physical interpretation of the optical model of a spatial filter system (SFS) is grounded in the

physical optics, a branch of optics, specifically, Fourier optics, where the positive lens functions as a Fourier transform from the lens itself to the focus point of the laser beam incident upon it [7].

In Figure 1a, a typical SFN is observed, with a microscope objective (MO) as a positive lens; a pinhole or spatial filter H as a low-pass filter; a second positive lens L with the function of an inverse Fourier transform for the retrieval of the transmitted wavefront [8]. The model's explication is as follows; a Gaussian wavefront, with its initial state at an infinite distance described by $F_0(x_0, y_0, -z)$ (collimated laser beam) and able to be in Z or in the (x_0, y_0) plane, is likely to have wavefront optical aberrations because of optical phenomena like diffraction and scattering.

To clean the wavefront, the SFS is implemented as follows:

$$U(w_x, w_y) = \mathcal{F}\{F_0(x_0, y_0)\}, \tag{1}$$

where $\mathcal{F}$ and U are the Fourier operator and its harmonics in (w_x, w_y) plane, respectively.

In the (w_x, w_y) plane, the noise of F_0 is composed by the high frequencies of U (red waves) and most of their information is constituted by low frequencies of the optical perturbation (blue wave), as shown in Figure 1a. If the high frequencies are blocked by a physical obstacle like the pinhole $H(w_x, w_y)$ one obtains the following equation:

$$U'(w_x, w_y) = H(w_x, w_y)U(w_x, w_y), \tag{2}$$

where U' represents the filtered Fourier spectrum of F_0.

To retrieve the clean wavefront, a positive lens L is placed at their focal distance f_L, and yield the inverse Fourier transform in (x_1, y_1) plane, so, the collimated and clean wavefront $G(x_1, y_1)$ is obtained by equation 3:

$$G(x_1, y_1) = \mathcal{F}^{-1}\{U'(w_x, w_y)\}. \tag{3}$$

To be able to see the wavefront in any plane, the intensity I of the wavefront in the same plane must be calculated, this through the calculation of the square of the magnitude of the desired observation, for example, for the (x_0, y_0) plane the equation is:

$$I(x_0, y_0) = |F_0(x_0, y_0)|^2, \tag{4}$$

and for the clean wavefront in plane (x_1, y_1) the intensity is:

$$I(x_1, y_1) = |G(x_1, y_1)|^2. \tag{5}$$

Figure 1b describes the functionality of a microscope objective (MO) when a collimated laser beam is incident upon it. The MO acts as a positive lens system, concentrating the light into a single focal point at f_{MO}.

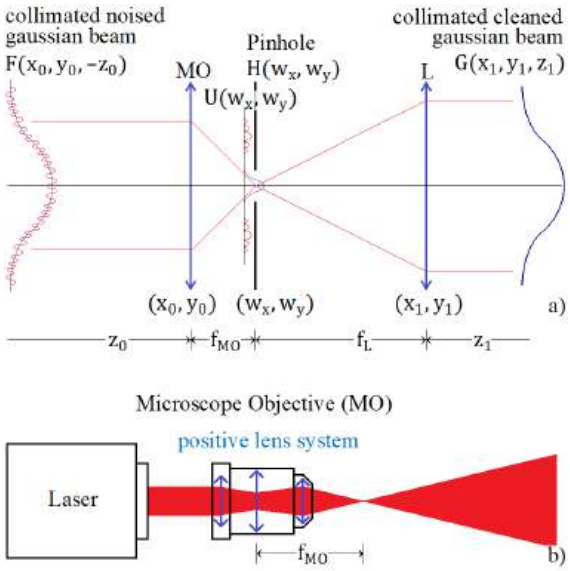

Fig. 1. Spatial Filter System: a) SFS optical set-up; b) microscope objective operation with collimated light input

The use of an SFS in optical metrology set-up produces a clean, uniform wavefront that is well-suited for applications like, for example, high-precision interferometric measurements.

3.2 Border Following

Is an algorithm based on the work [14]. This approach utilizes a scan of the binary mask to identify topological boundaries of connected components. The algorithm executes the following steps:

1. **Initialization:** Starting with a raster order scan (top-left to bottom-right), the algorithm searches the image for pixels than marks the start of an object's outer boundaries. This starting pixel is a non-background pixel adjacent to a background pixel.

2. **Iterative Border Following:** Once the initial coordinate is located, the process systematically follows the boundary. By evaluating the 8-connected neighborhood of the current pixel, the algorithm identifies the next adjacent pixel that forms part of the object's perimeter. The algorithm maintains a constant orientation when establishing the next coordinate in the sequence (clockwise or counter-clockwise) to ensure proper tracing of both outer and inner (hole) boundaries.

3. **Contour Closure:** This boundary-tracking sequence proceeds until the algorithm converges back on the initial coordinate, signifying the full delineation of the object's perimeter

4. **Exhaustive Search:** The algorithm continues scanning the image for any remaining unvisited object pixels. Upon encountering such a pixel, steps (b) and (c) are repeated to trace the contour of the newly found object. This continues until all object boundaries in the image have been identified.

3.3 Connected-component Labeling

Connected-component labeling (CCL) is an operation in image processing and computer vision, where the primary objective is to identify and label distinct connected regions within a binary image. The foundation of CCL algorithms lies in the concept of connectivity. In a binary image, two pixels are considered connected if they are adjacent to each other and have the same value (typically 1 for foreground pixels). This notion of connectivity can be further refined into 4-connectivity, where pixels are connected only if they share an edge, and 8-connectivity, where pixels sharing an edge or a corner are considered connected. The goal of CCL is to assign a unique label to each connected component, effectively distinguishing it from other components. One of the fundamental data structures used in many CCL algorithms is the UNION-FIND data structure, also known as the disjoint-set data structure. This structure efficiently maintains a collection of disjoint sets, each set represents a connected component, and the elements are the pixels. Initially, each pixel is in its own set. As the image is scanned, adjacent pixels with the same value are merged [4].

3.4 Simple Linear Iterative Clustering (SLIC)

The Simple Linear Iterative Clustering (SLIC) algorithm is a centroid-based clustering method used to generate superpixels. It groups pixels based on both color similarity and spatial proximity within the image plane. SLIC operates in a 5-dimensional space, combining the three color channels (l, a, b) and the two spatial coordinates (x, y) of each pixel, denoted as $[l, a, b, x, y]$. Because the color and spatial dimensions have different units and ranges, spatial distances are normalized to ensure accurate distance calculations using the Euclidean norm [2]. The algorithm takes as input the desired number of approximately equally sized superpixels, K for an image of N pixels. At initialization, K superpixel cluster centers $C_i = [l_i, a_i, b_i, x_i, y_i]^T$ placed on a regular grid, with an initial spacing of S where:

$$S = \sqrt{N/k} \tag{6}$$

This means that the approximate area of each superpixel is S^2. The SLIC algorithm then proceeds iteratively:

1. **Assignment Step:** For each pixel i, the algorithm is associated with the nearest cluster center.

2. **Update Step:** After all pixels have been assigned to a cluster, the new cluster centers are calculated as the mean vector $[l, a, b, x, y]^T$ of all pixels belonging to that cluster.

3. **Error Calculation:** The $L2$ norm of the difference between the new cluster centers and the previous cluster centers is computed

The assignment and update steps are repeated iteratively until the error converges or a maximum number of iterations is reached. In practice, 10 iterations are typically sufficient for convergence.

4 Methodology

The present work aims to compare different well-established algorithms for machine vision. The comparison of algorithms is based on two key metrics: processing speed and detection error. The procedure for alignment relies on evaluating the Airy diffraction pattern produced by the pinhole. The theoretical framework for circular apertures permits approximating the pattern's intensity profile with a 3D Gaussian distribution. The X-Y-Z coordinates of the laser beam's center are assumed to correspond to the peak point of this Gaussian distribution. The distribution of the Airy pattern is in Figure 2.

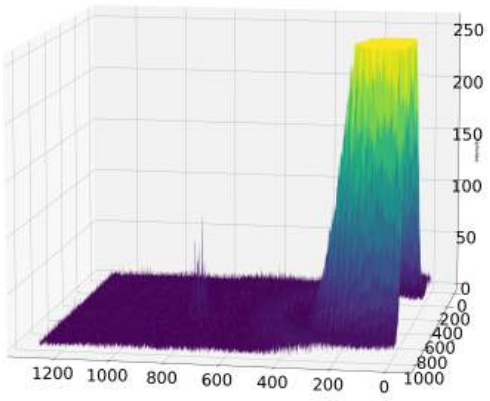

Fig. 2. Intensity distribution from a dataset's image

Conventional centroid detection methods including maximum intensity search, Gaussian/Bessel fitting, and radial profiling were excluded from direct comparison. These methods often lack robustness in non-ideal scenarios (such as occlusion or high dispersion and diffraction scenarios) or require circular dependencies like, for example, needing a center estimate to calculate a radial profile. Therefore, we selected composite 'hybrid' algorithms or image processing pipelines to measure their performance. Specifically, we implemented Fixed-Threshold Border Following with Moments (FBM), Otsu-based Connected Component Labeling (CCL), and superpixels segmentation with maximum intensity search, as these methods fuse segmentation with geometric analysis to provide the necessary robustness.

To determine the centroid, the performance of the following algorithms will be evaluated and compared:

— **Connected-Component Labeling:** From the scikit-image Python library, this method identifies and labels connected regions in the image, allowing for centroid calculation of the largest connected component, which fuses adaptive Otsu thresholding with graph-based connectivity analysis and morphological filtering to robustly isolate and calculate the centroid of the largest coherent region.

— **Fixed-Threshold Border Following with Moments :** Using the Python cv2 (OpenCV) library, algorithm traces the boundary of the Airy pattern and calculates its spatial moments. The peak point is derived from these moments. The algorithm integrates Gaussian blurring for denoising, fixed binary thresholding, morphological closing, and topological contour tracing to derive geometric moments.

— **Superpixel Clusters with SLIC, Quickshift and Felzenszwalb:** From the Scikit-image Python library, the SLIC, Quickshift and Felzenszwalb algorithms groups pixels into meaningful regions (superpixels) using the color and spatial proximity of the pixels. After the segmentation of the image, based on the Airy pattern theory, the segment with the maximum intensity is selected as the peak segment and the centroid is calculated based on the maximum pixel values of the segment before superpixel algorithms are applied. For each of the superpixels algorithms, after segmentation and a 3 pixels kernel Gaussian

blur, a vectorized statistical aggregation computes the mean intensity for each region, the algorithm computes the mean intensity for every generated superpixel. It then identifies the ”target” as the specific superpixel that maximizes the average intensity of the scoring channel, prioritizing the brightest object rather than the brightest pixel. The region of interest is identified via a maximum intensity search, and once the target superpixel is isolated, calculates the spatial center of mass with the first-order spatial moments of the selected segment's binary mask.

Each superpixel algorithm requires its own set of hyperparameters, prioritizing a lower error, for the Felzenszwalb the relevant hyperparameter selection was a value for scale parameter (λ) equal to 200, sigma for a Gaussian kernel equal to 0.5 and a minimum pixel size for an element of 150, for the QuickSifth the values are a Gaussian kernel size of 21, a maximum data distance equal to 50 and a color -spatial ratio value equal to 5. Finally, for SLIC a different approach was selected, depending of the wavefront, a different value of initial segment size k was selected, 100 initial segments for green and blue wavefronts and 30 for red.

The algorithms under test will be implemented and evaluated using images captured from an actual optical spatial filter, images taken at multiple wavelengths, 635nm, 520, 405nm (Thorlabs PL202, PL201 and PL205).

4.1 Computational Set up

The experiments were conducted on an old entry-level laptop running Manjaro Linux (Arch Linux based), equipped with an AMD Ryzen 3 2200U processor, comparable to a Raspberry Pi 5, (a geek bench score of 1506 for the Raspberry Pi 5 and 1596 for the Ryzen) and 12 GB DDR4 RAM at 2600 MT/s. To promote reproducibility and maintain a consistent and low-conflict software environment, the experiments were conducted within a Docker container derived from the official *python:3.10-alpine* image hosted on Docker Hub. This containerization strategy effectively isolated the execution environment, mitigating the risk of conflicts with system-wide libraries or configurations. This setup aims to compare the algorithms in a low performance hardware; a more capable hardware was tested in [11].

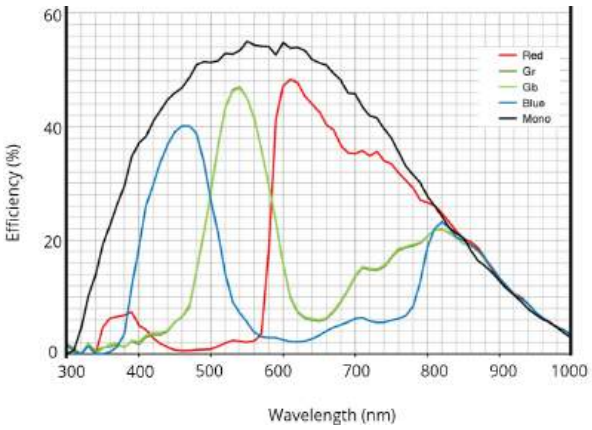

Fig. 3. Quantum efficiency of the FLIR CCD camera

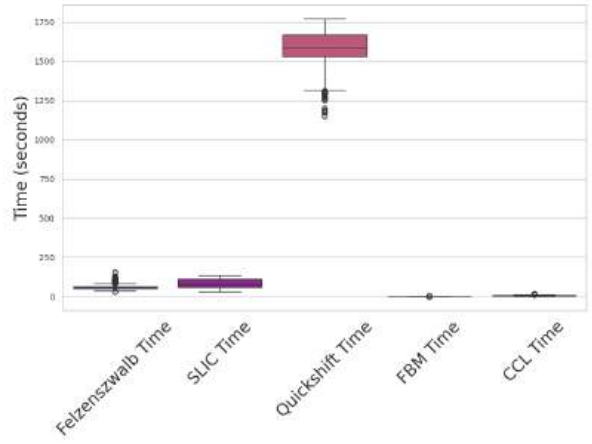

Fig. 4. Processing times running in a Ryzen 2200U for each of the algorithms under test

4.2 Dataset

A FLIR Blackfly S BFS-U3-13Y3M-C CCD camera (1280 x 1024 pixels, 10-bit depth) was implemented after the pinhole to acquire images of the Airy patterns and the subsequent dataset creation, Figure 3 displays the quantum efficiency of the

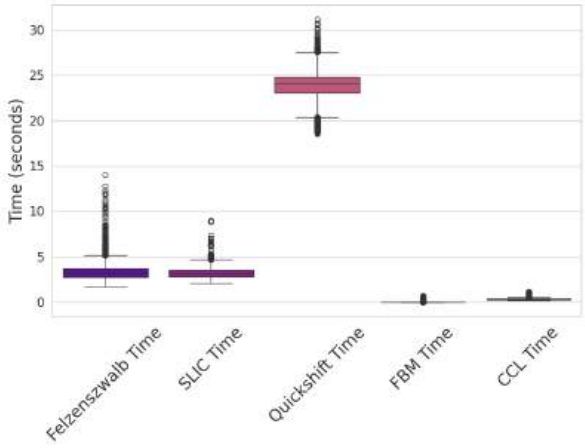

Fig. 5. Processing times running in a Ryzen 5600X [11] for each of the algorithms under test

CCD camera, where each of the Thorlabs PL202, PL201 and PL205 wavelengths is contained by the camera RGB peak values. A 50 mm focal LB1471-A bi-convex lens between the camera and the pinhole sensor. A Newport M-40X microscope objective and an Edmund Optics 10μm diameter pinhole was used. Images were taken using motorized linear stages to simultaneously move the pinhole and the attached CCD camera, effectively moving the laser beam across the pinhole and, consequently, across all the CCD camera sensor.

The optical arraignment was divided into two independent and fully aligned modules, the laser beam and the microscope objective as the module number one and the CCD camera and the pinhole as the second and movable module making the intensity pattern's movement dependent only to relative position of the pinhole respects to the microscope objective.

The final dataset was divided into two subsets: for evaluating total processing time for each image and algorithm and the other quantifying detection error.

Subset 1 (Processing Time): This subset consisted of 16,499 images, each capturing varied laser spot positions across the full extent of the CCD sensor. The dataset was designed to ensure a diverse array of input conditions to evaluate algorithm's computational efficiency. A motorized stage was employed to systematically displace the laser spot across the sensor.

Subset 2 (Error measure): Drawn from Subset 1, this subset contained 493 images stratified across 29 general laser spot positions. The "true" peak point of each laser Airy pattern was manually identified and recorded, providing the "truth" for evaluating centroid estimation accuracy. The "true" peak point was obtained by the Airy disk Intensity function following the Fraunhofer diffraction pattern of a circular aperture, given by the squared modulus of the Fourier transform of the circular aperture in a binarized image with a threshold in values of 254. The Euclidean distance between the true and algorithm-calculated peak points was employed as the quantitative error metric.

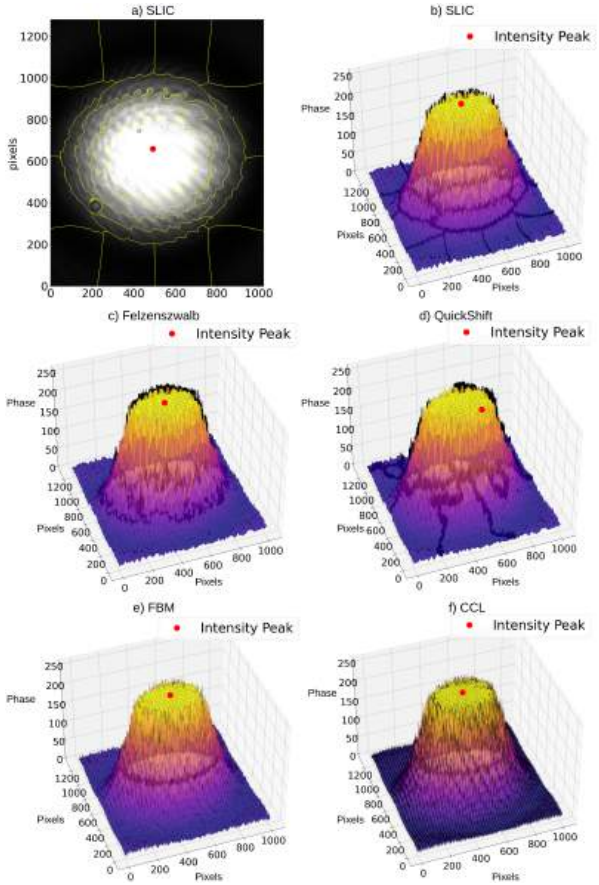

Fig. 6. Peak intensity point for each algorithm in a fully contained scenario

5 Results

In Figure 4, illustrates the processing time required by each algorithm on test subset 1 for the Ryzen 2200U. The results reveal a pronounced disparity in execution time between the superpixel-based algorithms and the baseline methods (CCL and FBM).

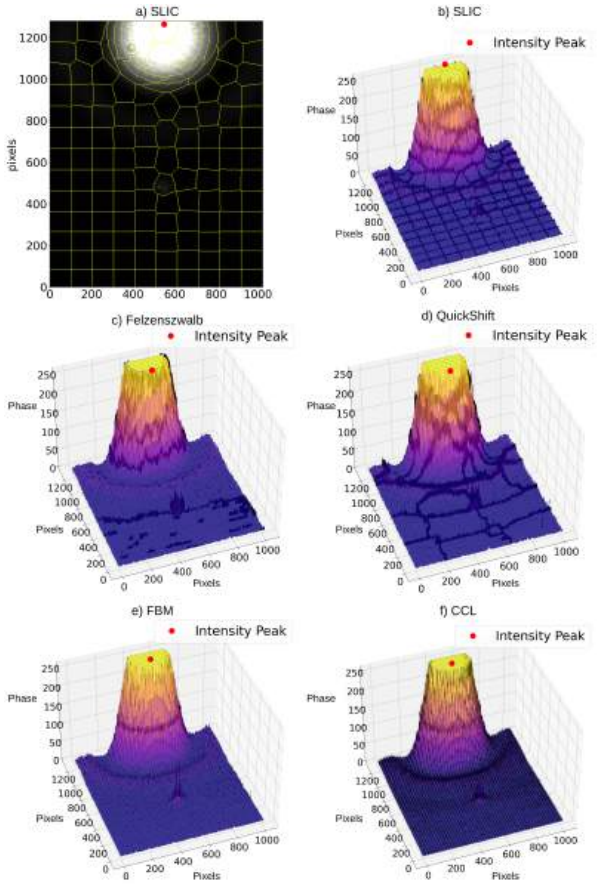

Fig. 7. Peak intensity point for each algorithm in a middle-place scenario

On average, the superpixel algorithms exhibited significantly higher computational demands, operating approximately 862 times slower than FBM and 77 times slower than CCL with an avereage of 572.4942564 seconds.

The average execution time for the superixel algorithms was heavily skewed by the Quickshift algorithm, which demonstrated a significantly longer execution time compared to the SLIC and Felzenszwalb algorithms. Excluding the Quickshift algorithm from the calculation, the mean processing time was reduced to 72.000344 seconds. The SLIC and Felzenszwalb algorithms were 94.74 % and 96.11 % faster than the Quickshift algorithm, respectively.

Taking the average time of the superpixel algorithms without Quickshift, the compassion with the CCL and FBM results in CCL 89.7 % faster, and FBM remained 99.07 % faster.

In order the SLIC, Felzenszwalb, Quickshift, FBM and CCL, the average precessing times are 82.77523256, 61.22545544, 1573.482081, 0.6641959113, 7.418052648 seconds.

A comparative analysis of execution times reveals a significant performance discrepancy among the tested algorithms. The FBM and CCL methods consistently exhibited superior computational efficiency compared to the superpixel algorithms. While superpixel algorithms offer distinct advantages in representing image structure for specific applications, their slower processing times are a notable limitation. The heterogeneity within the superpixel class is particularly evident, with the Quickshift algorithm exhibiting a significantly higher execution time than its counterparts, SLIC and Felzenszwalb. Even the fastest superpixel method remains considerably slower than both FBM and CCL. This outcome suggests that FBM is a particularly competitive solution when the processing time efficiency is important.

Also, a comparative with [11] shows the performance gap between the different hardware configurations. Some algorithms considered suitable for real time controllers aren't a viable solution for hardware components like the Ryzen 2200U. For example, the execution of the SLIC algorithm on a Ryzen 5 5600X CPU required an average of 3.180172493 seconds, while the same on a Ryzen 3 2200U CPU took 82.77523256 seconds, a performance difference of 79.595060067 seconds. Figure 5 shows the Ryzen 5 5600X processing times.

While the lower processing time of the FBM and CCL compared to superpixel algorithms is an advantage, it's not the only performance metric.

Centroid accuracy, which directly impacts the precision of downstream control systems, is critically important. This section analyzes the centroid estimation error of the SLIC, Felzenszwalb, and Quickshift superpixel algorithms in comparison to the FBM and CCL. Figure 6 and 8 illustrates the peak intensity point estimation performance when the diffraction pattern is fully contained within the CCD camera sensor's field of view.

For the analysis under ideal conditions where the spatial filter is fully aligned, 17 images derived from the subset 2, which itself stems from subset 1, corresponding to this ideal conditions, both FBM and CCL demonstrate superior accuracy. FBM achieved an average Euclidean distance error of 4.47 pixels, and CCL had an average error of 4.74 pixels. In contrast, the superpixel algorithms exhibited significantly higher errors: SLIC (5.01 pixels), Felzenszwalb (61.13 pixels), and Quickshift (84.97 pixels). Demonstrating advantage for FBM and CCL for scenarios where the entire diffraction pattern is captured.

However, the relative performance of the algorithms shifts dramatically when the diffraction pattern is partially occluded, i.e., when the spot is located at the border of the sensor. Figure 7 represents results for 1 of the 29 classes from Subset 2, representing instances where the laser beam is positioned between the periphery and the center of the sensor.

Figures 10 and 9 represents where is border-case scenarios, here, Quickshift and Felzenszwalb show a marked improvement in accuracy, with average peak point detection errors of 19.69 pixels and 12.74 pixels, respectively.

SLIC's performance degrades to an average error of 45.01 pixels, while FBM and CCL exhibit significantly increased errors of 143.84 pixels and 137.82 pixels, respectively.

The results indicate that Quickshift and Felzenszwalb demonstrate superior robustness when dealing with incomplete diffraction patterns. This resilience stems from their focus on identifying intensity peaks, even local ones.

In contrast, FBM and CCL rely on centroid calculations which, when applied to truncated intensity distributions, can result in misleading localization.

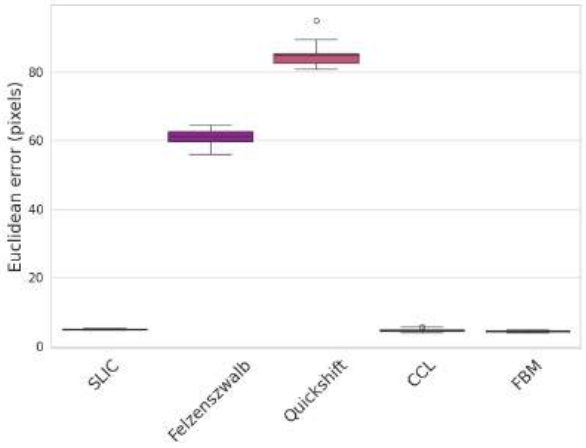

Fig. 8. Euclidean error for scenarios where the laser beam is focusing into the center of the CCD camera sensor

6 Conclusions

Our findings reveal that the algorithm with a fixed threshold and border following plus Moments (FBM) and Connected Component Labeling (CCL) algorithms are the most promising candidates for applications requiring high-speed peak intensity point determination like for example, controllers where the time is crucial or applications where a long time misalignment are not tolerated. FBM, in particular, demonstrated the shortest execution times in the order of ms, making it uniquely suited for real-time control applications where latency is a critical requirement while the detection error remains high in border scenarios and low for the corrected alignment scenarios, all in compassion with superpixels algorithms.

Despite the generally higher execution times of superpixel algorithms, the SLIC algorithm provided the most consistent accuracy among the tested methods. On desktop equipment, specifically the Ryzen 5600X CPU, SLIC also demonstrated a relatively low execution time, making it a reliable option when consistency is the primary objective. However, its performance on embedded or portable hardware is not sufficient for real-time control applications.

A notable advantage of SLIC is its ability to estimate cluster size, which can be leveraged

to refine the center detection of Airy patterns in different positions and wavelengths.

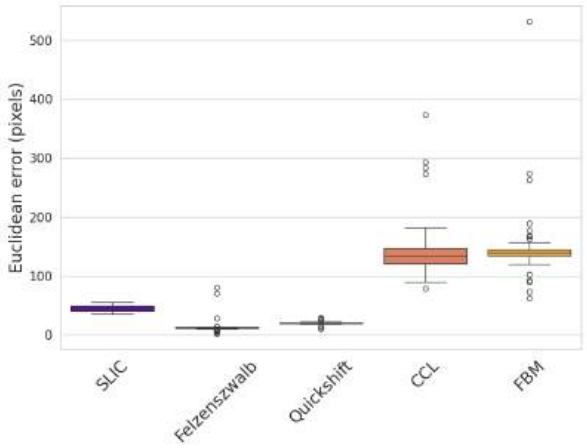

Fig. 9. Euclidean error for scenarios where the laser beam is focusing into the border of the CCD camera sensor

This study provides an empirical framework for selecting appropriate machine vision algorithms for auto-aligned spatial filters.

Due to their superior speed, Fast Block Matching (FBM) and Connected Component Labeling (CCL) algorithms are particularly well-suited for systems with low computational resources, such as portable or embedded platforms, where rapid response is critical.

Conversely, the Simple Linear Iterative Clustering (SLIC) algorithm provides a valuable alternative for applications where reliability and cluster-size estimation are paramount, as it maintains consistently low processing times relative to other superpixel methods.

As future work, we should investigate hybrid pipeline approaches that dynamically switch between algorithms like SLIC and the faster FBM or CCL to optimize for both processing time and accuracy.

The latter seeks a system fast enough for real-time portable embedded systems to perform optical spatial filtering with precision and accuracy, which is required in optical systems for interferometry, holography, non-destructive optical testing, optical applications in biomedicine, etc.

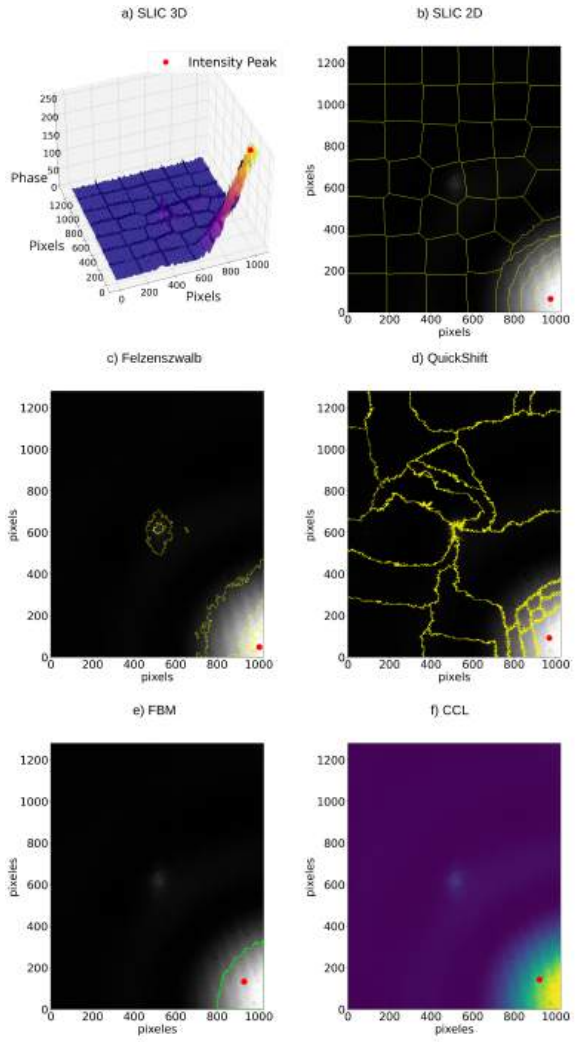

Fig. 10. Peak intensity point for each algorithm in a border-case scenario

Acknowledgments

The authors acknowledge financial support from the *Programa de Apoyo a la mejora en las condiciones de producción de los miembros del SNII y SNCA* (PROSNII grants 2023 and 2024). And also MC Gregorio A. Oropeza-Gomez would like to acknowledge financial support through a scholarship from SECIHTI, CVU 1317498.

References

1. **Abramovici, A., Althouse, W. E., Drever, R. W. P., Gürsel, Y., Kawamura, S., Raab, F. J., Shoemaker, D., Sievers, L., Spero, R. E., Thorne, K. S., Vogt, R. E., Weiss, R., Whitcomb, S. E., Zucker, M. E. (1992).** Ligo: The laser interferometer gravitational-wave observatory. Science, Vol. 256, No. 5055, pp. 325–333. DOI: 10.1126/science.256.5055.325.

2. **Achanta, R., Shaji, A., Smith, K., Smith, K., Lucchi, A., Fua, P., Süsstrunk, S. (2012).** Slic superpixels compared to state-of-the-art superpixel methods. IEEE Transactions on Pattern Analysis and Machine Intelligence, Vol. 34, pp. 2274–2281.

3. **Cui, W., Zhu, J., Liu, Z., Fan, Q., Jiao, Z., Zhang, J., Lin, W., Dong, Z. (2021).** Optomechanical coupling active control for improving beam pointing accuracy of the spatial filter in pw laser facility. Applied Sciences (Switzerland), Vol. 11. DOI: 10.3390/app11115017.

4. **Dillencourt, M. B., Samet, H., Tamminen, M. (1992).** A general approach to connected-component labeling for arbitrary image representations. Journal of the ACM (JACM), Vol. 39, pp. 253–280.

5. **Gawali, S., Medina, J., Gailevičius, D., Purlys, V., Garre-Werner, G., Cojocaru, C., Trull, J., Botey, M., Herrero, R., Montiel-Ponsoda, J., Staliunas, K. (2020).** Spatial filtering in edge-emitting lasers by intracavity chirped photonic crystals. J. Opt. Soc. Am. B, Vol. 37, No. 10, pp. 2856–2864. DOI: 10.1364/JOSAB.397005.

6. **Gómez, G. A. O., Orozco-López, J. O., Casillas-Rodríguez, F. J., Mora-Gonzalez, M. (2022).** 2d automatic alignment of optical spatial filtering system by pid control. 2022 IEEE International Autumn Meeting on Power, Electronics and Computing (ROPEC), IEEE, Vol. 6, pp. 1–6.

7. **Goodman, J. W. (2005).** Introduction to Fourier optics, 3rd ed. Roberts and Company publishers.

8. **Klein, M. V. (1970).** Optics. John Wiley & Sons, Inc.

9. **Li, S., Yang, K., Ding, L., Zhou, L., Wang, Y., Wang, Y., Lu, Z. (2017).** Beam alignment based on the imaging properties of the spatial filter by controlling the deformable mirror in a high power laser. Optik, Vol. 142, pp. 205–210. DOI: https://doi.org/10.1016/j.ijleo.2017.05.101.

10. **Oropeza-Gomez, G. A., Orozco-López, J. O., Casillas-Rodríguez, F. J., Peña-Lecona, F. G., Muñoz-Maciel, J., Mora-Gonzalez, M. (2025).** High-precision spatial filtering with ai-driven control and multicolor laser testing for interferometric application. Integration, Vol. 103, pp. 102406. DOI: 10.1016/j.vlsi.2025.102406.

11. **Oropeza-Gomez, G. A., Orozco-López, O., Casillas-Rodríguez, F. J., Peña-Lecona, F. G., Muñoz-Maciel, J., Mora-Gonzalez, M. (2025).** Laser beam centroid detection for automatic spatial filtering: a comparative analysis of machine vision algorithms. Pattern Recognition. MCPR 2025. Lecture Notes in Computer Science, Springer, Berlin, Heidelberg, Vol. 15715, pp. 234–244.

12. **Sasaki, M., Arai, Y., Kamada, W., Hane, K. (1998).** Improved automatic alignment of pinhole integrated with photodiode. Japanese Journal of Applied Physics, Vol. 37, pp. 7120–7123.

13. **Sharma, A. K., Patidar, R. K., Daiya, D., Joshi, A., Naik, P. A., Gupta, P. D. (2013).** Simple and sensitive technique for alignment of the pinhole of a spatial filter of a high-energy, high-power laser system. Appl. Opt., Vol. 52, No. 12, pp. 2546–2554. DOI: 10.1364/AO.52.002546.

14. **Suzuki, S., be, K. A. (1985).** Topological structural analysis of digitized binary images by border following. Computer Vision, Graphics and Image Processing, Vol. 30, pp. 32–46.

15. **Wang, Y., Zhai, H., Jutamulia, S., Mu, G. (2007).** Collimation test of a corrected laser diode beam using lateral shearing interferometer. Optics Communications, Vol. 274, No. 2, pp. 412–416. DOI: https://doi.org/10.1016/j.optcom.2007.02.039.

16. **Weng, J., Zhong, J., Hu, C. (2010).** Automatic spatial filtering to obtain the virtual image term in digital holographic microscopy. Appl. Opt., Vol. 49, No. 2, pp. 189–195. DOI: 10.1364/AO.49.000189.

17. **Xiao, Z., Han, D., Zhu, H., Wang, L., Xu, Z. (2016).** Research on automatic focusing technique based on image autocollimation. Optik, Vol. 127, No. 1, pp. 148–151. DOI: https://doi.org/10.1016/j.ijleo.2015.10.037.

18. **Zhang, D., Dong, Z., Zhang, C., Liu, Z., Zheng, L., Pang, X., Zhu, J. (2022).** Investigation on parallel auxiliary adjusting machine of spatial filter lens for a high-power laser facility. Optics and Laser Technology, Vol. 147, pp. 107597. DOI: https://doi.org/10.1016/j.optlastec.2021.107597.

Article received on 25/08/2025; accepted on 09/12/2025.
**Corresponding author is Miguel Mora-Gonzalez.*